3-D-Printing-Based Selective-Ink-Deposition Technique Enabling Complex Antenna and RF Structures for 5G Applications up to 6 GHz

Valentina Palazzi, *Member, IEEE*, Wenjing Su, *Member, IEEE*, Ryan Bahr, *Student Member, IEEE*,
Silvia Bittolo-Bon, Federico Alimenti, *Senior Member, IEEE*, Paolo Mezzanotte, *Member, IEEE*,
Luca Valentini, Manos M. Tentzeris, *Fellow, IEEE*, and Luca Roselli, *Fellow, IEEE*

Abstract— This paper introduces a novel additive-manufacturing technique to obtain high-resolution selective-ink-deposition on complex 3-D objects, packages, and modules for 5G applications. The technique consists of embossing the desired pattern directly on the 3-D printed dielectric surface and then applying ink with a suitable tool. This approach is tested in combination with stereolithography 3-D printing technology to obtain selectively metallized 3-D circuits. In particular, the "clear" resin from FormLab is utilized for the 3-D printed dielectric, while the metallization is performed with silver nanoparticle ink from Suntronic. As a preliminary study, test samples containing lines with different widths are manufactured, demonstrating a pitch down to 135 μm and satisfactory sheet resistance of 0.011 Ω/sq. (the electromagnetic characterization of the dielectric resin is reported in the Appendix). Then, two broadband multiport RF structures are developed to show the versatility of the proposed technology. First, an ultrawideband 3-D crossover, operating in the range 100 MHz–5 GHz, is conceived to test the suitability of the proposed technology to perform selective metallization on curved semienclosed areas. Then, the technology is applied to a multiple-input–multiple-output (MIMO) antenna system, based on four proximity-fed annular slot antennas, arranged on the lateral sides of a cube and decoupled by introducing a cross-shaped structure in the interior of the cube. This circuit offers a broad range of metallization challenges, as it features embossed and engraved parts, high-resolution patterns (line widths down to 0.7 mm) and sharp edges. Each slot radiates unidirectionally with the same polarization and uses the cube and its internal cross-shaped structure as a resonant cavity. The antenna system is designed to operate in the band 3.4–3.8 GHz, which is one of the sub-6-GHz 5G bands in Europe, and it is thought for hotspot and access-point applications. The final antenna topology is composed of only two blocks, weighs 21.29 g, and occupies a volume of 44.4 × 45.8 × 45.8 mm^3, featuring an envelope correlation coefficient (ECC) lower than 0.005 and a total active reflection coefficient (TARC) lower than −6 dB in all the bands of interests.

Index Terms— 3-D printing, 5G, additive manufacturing, broadband antennas, Internet of Things, multiple-input–multiple-output (MIMO) antennas, slot antenna cube, stereolithography.

I. INTRODUCTION

IN THE upcoming 5G era, wireless communications will become ever more ubiquitous and pervasive [1], [2]. Different systems with heterogeneous needs in terms of number and type of users, bandwidth, and read range will be established. Everyday objects equipped with suitable transponders will interact with each other in variable environments [3]–[5]. Techniques, such as "space division multiple access" [6] and multiple-input–multiple-output (MIMO) systems [7]–[10], will enable simultaneous communications utilizing the same frequency bands. This calls for the adoption of broadband multiport RF components.

Recently, research has focused on the optimization of MIMO antenna topologies for wireless portable devices, such as mobile phones, hotspots, and access points [11], [12]. Antennas arranged on the sides of 3-D polygons are proposed to implement MIMO antenna topologies with improved scanning ability [17]–[22]. Unfortunately, traditional low-cost circuit prototyping techniques are typically optimized for planar structures. Consequently, every time the third dimension needs to be exploited, fabrication processes become complex and expensive, as shown in Table I. The structure must be split into multiple parts, shaped by adopting techniques, such as laser machining and drilling, and assembled by using screws, soldering techniques, and so forth. Sometimes, the resulting prototype can be heavy, fragile, and unstable. In all of the reported cases, the mutual coupling between copolarized radiating elements is higher than −15 dB, while lower values are obtained placing adjacent elements in orthogonal polarization.

Ref.	Description	Fabrication
[17]	Six aperture-coupled patch antennas orthogonally polarized arranged on the lateral sides of a pyramidal metal structure working at 5 GHz.	Each antenna is individually fabricated in a multi-layer thick substrate and is mounted with screws on a hollow trucated hexagonal pyramidal metal structure with grooves.
[18]	Cube with three orthogonal rectangular slots working at 5.85 GHz. The antennas utilize the cube as a cavity and are fed with shortened probes, featuring an impedance bandwidth of 2 %.	Metal shell made of two pieces of bronze soldered together; slot and probes manufactured with laser sintering. The cavity is filled with a CNC machined block of Teflon, while holes are drilled to accommodate probes.
[19]	24-port and 36-port antenna cubes based on cross-polarized quarter-wave and half-wave slots operating at 2.7 GHz	"joint" approach: high number of 2D building components made of FR4 PCB. Slits are milled out, while the antenna forms are etched.
[20]	20 dual-polarized inverted-F antennas operating in the frequency range $2.4 - 2.8$ GHz suspended on 5 sides of a cube (4 elements for each side).	Antennas made of curved pieces of metal on an FR4 PCB substrate. Shorting pins are attached to the radiating edges opposite to the feed points. Their localized ground plane is etched from the PCB. The cube is formed by connecting five PCB sides with screws.

In this a scenario, additive-manufacturing techniques, including nonmetallic 3-D printing, such as fused deposition modeling and stereolithography, and metallic 3-D printing, such as binder jetting and selective laser melting, can enable easy, low-cost, and scalable fabrication of arbitrarily shaped circuits, as reported in the literature [23]–[30]. For instance, metallic 3-D printing has been used to manufacture waveguide-based antennas and RF components up to terahertz frequencies [23], [24]. This approach makes it possible to realize one-piece metallic components, thereby reducing assembling time, and it requires only minimal postprocessing (limited to surface polishing). On the other hand, nonmetallic 3-D printing has been used to realize both the dielectric scaffolding for lightweight waveguide-based components (the 3-D-printed parts are completely metallized with techniques, such as electroless plating) and to manufacture dielectric parts of the circuit, such as dielectric lens, substrates, and packages [25]–[30].

A residual difficulty associated with nonmetallic 3-D printing is the realization of high-resolution metal patterns on arbitrarily shaped dielectric objects. At present, ink-jet printing and microdispensing are utilized for planar surfaces, while expensive tools, such as aerosol-jet printers, are used to perform metal patterns on more complex objects.

This paper aims to overcome the aforedescribed limitations by proposing an embossed surface patterning technique. The proposed methodology is then applied to two broadband multiport RF structures developed to show the versatility of the proposed technology: a 3-D microstrip-line crossover and 3-D MIMO cube antenna topology. The cube features an internal 3-D printed structure that is utilized to place adjacent antennas in vertical polarization (same polarization can be useful in beam-steering applications) while obtaining a satisfactory isolation, bandwidth, and volume occupation. At the same time, high robustness is achieved by minimizing the number of parts to be assembled, which combines with lightweight and reduced costs.

In Section II, the proposed fabrication process is outlined. In Section III, the technique is applied to a 3-D crossover, while Section IV reports the design process and the obtained experimental results of the proposed antenna topology. Finally, the conclusions are drawn in Section V.

II. MANUFACTURING PROCESS

The proposed additive manufacturing process aims to enable the fabrication of 3-D microwave circuits by relying on a single 3-D printing tool. In particular, embossed/engraved patterns, realized on arbitrary surfaces of 3-D printed objects, are harnessed to yield high-resolution ink patterns. Although this paper focuses on manufacturing conductive traces, the process can be easily applied to any kind of ink. This technology is presently tested with stereolithography 3-D printing. In stereolithography, 3-D objects are manufactured by laser curing liquid photoreactive resins. This approach is, here, preferred to other 3-D printing techniques for its low surface roughness and high resolution.

The experimental activity is carried out by using the Form 2 3-D printer [31], and the chosen photoreactive material is the so-called "clear" liquid resin from Formlabs. A preliminary electromagnetic (EM) characterization of the used material is conducted, and the adopted procedure is reported in the Appendix. The characterization includes testing multiple samples, to verify the consistency of the EM properties between one sample and the other. A measured dielectric constant ϵ_r of 2.8 and a tanδ of 0.03 have been obtained. It is worth noticing that the EM properties of the material (especially loss) depend on the curing profile (see [32]), so a limited variability in the dielectric properties after the metallization procedure (which involves curing steps) is expected.

Given the 3-D nature of the considered designs, standard approaches, such as ink-jet printing, are not applicable to perform selective metallization. Therefore, an alternative technique has been developed, and its schematic process is shown in Fig. 1.

In the proposed manufacturing process, the areas of the 3-D-printed dielectric "scaffolding" destined for ink deposition are extruded with respect to the others (i.e., the feedlines are embossed with respect to the rest of the surface, while slots are engraved), thereby obtaining an embossed surface patterning, as shown in Fig. 1(a). This can be readily achieved with 3-D printing at the design level. Then, metallization can
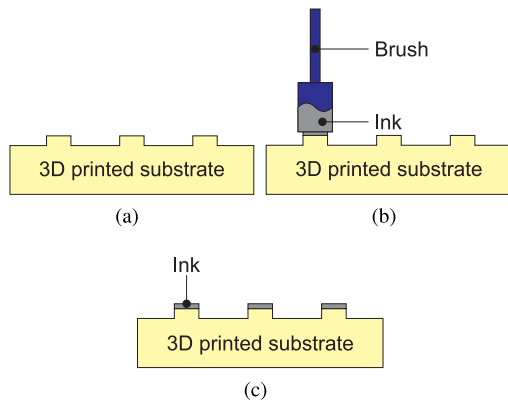
Fig. 1. Schematic process of the proposed 3-D-printing-based manufacturing technology. (a) 3-D-printed embossed surface. (b) Ink application. (c) Complete prototype with selective ink deposition.
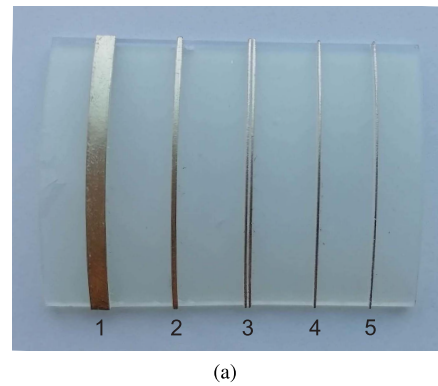

Fig. 2. Proposed manufacturing process applied to lines of different width on a curved surface: (a) top view and (b) perspective. Nominal linewidth: 1) 2 mm; 2) 0.5 mm; 3) two 0.2-mm-width lines separated by 0.3 mm; 4) 0.2 mm; and 5) 0.1 mm.
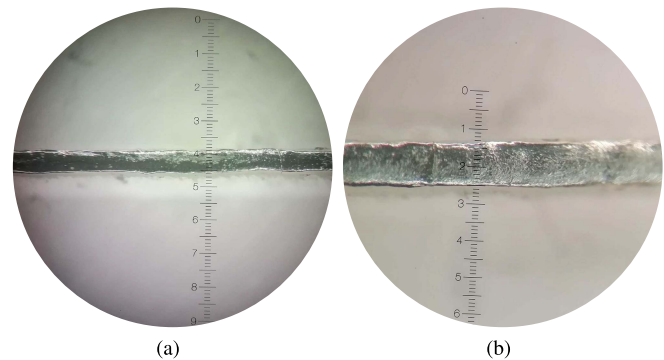

Fig. 3. Line view at microscope: (a) linewidth: 0.135 mm and (b) linewidth 0.237 mm. The width of each scale division has been calibrated with a stage micrometer and is equal to 21.5 μm.
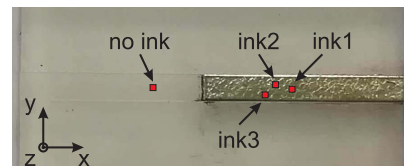

Fig. 4. Test sample with a line on a flat surface, where only a portion of the line is covered with ink. Linewidth: 2 mm. The areas analyzed with the AFM are marked in red.

be achieved by applying conductive ink (in this case, silver nanoparticle ink from Suntronic is utilized) to the protruding parts with a suitable tool, such as a brush or a cotton swab, as shown in Fig. 1(b).

To avoid overflow issues, low-viscosity inks must be utilized (the adopted silver ink has a viscosity of 11–15 cP), and the brush must be loaded with a small amount of ink. The latter quantity can be controlled by optimizing the immersion time of the brush in the ink bottle and removing excess ink. The brush bristles must be applied parallel to the embossed parts so that the brush area in contact with the pattern is almost flat and unwanted areas are not touched. That way, only the protruding areas are covered with ink [see Fig. 1(c)]. To keep control of the ink thickness, the brush must be moved with uniform pressure and must be loaded with a constant amount of ink. The chosen silver ink is cured at 110 °C for 10 min (a tradeoff has been performed between the ideal curing temperature of the ink, which is around 150 °C, and the heat deflection temperature of the resin, which is around 73 °C), and the procedure is repeated four/five times to achieve a satisfactory conductivity for the metal traces.

The resolution of the proposed ink deposition technology depends on the resolution of the 3-D printing process. The adopted stereolithography 3-D printing process features a minimum resolution step of 25 μm. The pitch is tested by manufacturing line patterns with different widths on a curved surface, as shown in Fig. 2. The minimum nominal linewidth of 100 μm has been tested in line 5. Lines 4 and 5 are inspected with a stereomicroscope equipped with a reticle (model Stemi SV 11 from Zeiss [33]), and their measured width is shown in Fig. 3. Both lines feature a constant width. Line 5 features a width of 135 μm, while line 4 features a width of 237 μm. The higher percentage error of the former line with respect to the latter is due to the fact that the width of line 5 is close to the resolution of the 3-D printing technology.

Surface roughness is also checked. To this purpose, an embossed line on a flat surface is manufactured, as shown in Fig. 4. Part of the sample has been covered with tape so that ink is deposited only on a portion of the line. An atomic force microscope (AFM, model easyScan DFM from Nanosurf) is then used to measure the surface roughness of the 3-D printed

sample with and without ink. AFM instrument operates in tapping mode using silicon cantilever. All the AFM images are produced by keeping the scan speed and scan size (i.e., 70 × 70 μm^2) constant. Four areas are scanned along the embossed line, which are marked with red boxes in Fig. 4. The first measurement is performed in an area without ink to check the surface roughness of the 3-D printed substrate alone. The measurement results are shown in Fig. 5. Fig. 5(a)
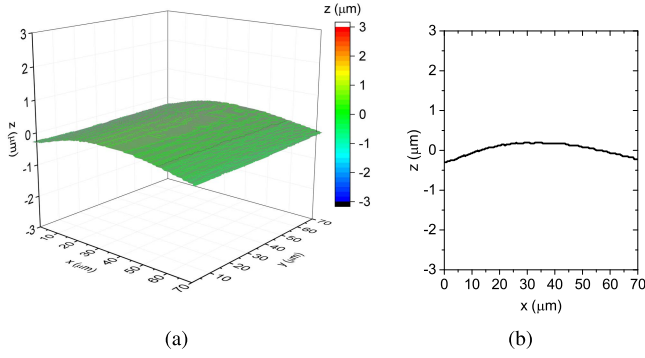
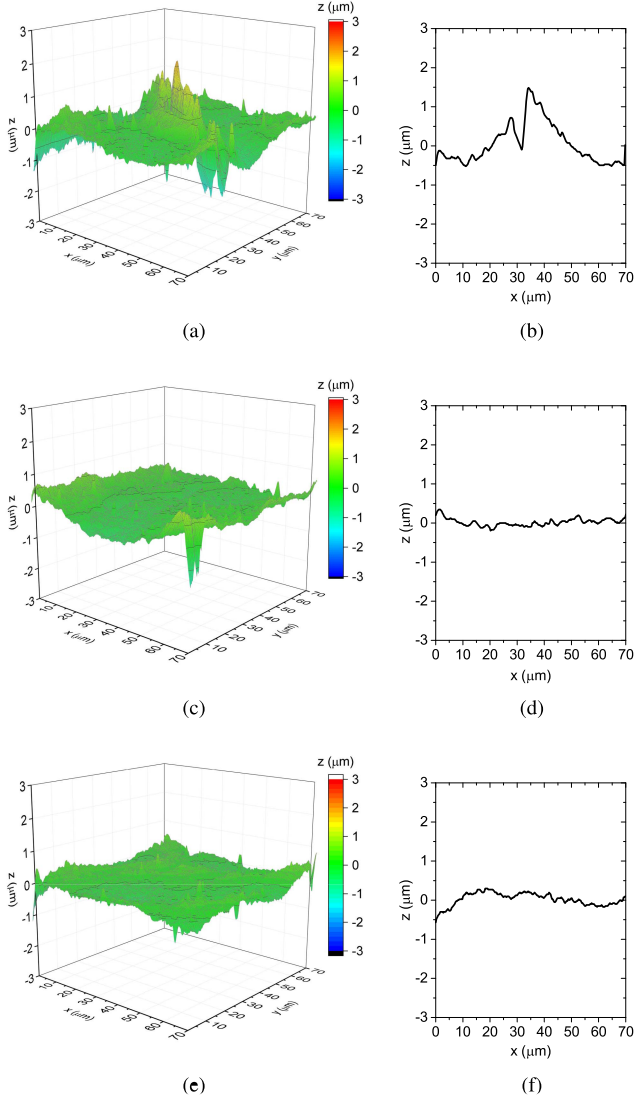Fig. 5. 3-D-printed area without ink. (a) AFM surface topography. (b) Scan profile recorded at $y = 35$ μm.

Fig. 6. (a), (c), and (e) AFM surface topography and (b), (d), and (f) scan profiles (recorded at $y = 35$ μm) of 3-D printed areas with ink.

shows the surface topography with AFM, while Fig. 5(b) reports the surface profile along a profile line at $y = 35$ μm. The line covered with ink, instead, is analyzed in three different areas to evaluate the ink uniformity. Fig. 6 shows the obtained results. Table II reports average surface roughness S_a, maximum peak height S_p, and maximum pit height S_v, for

TABLE II
AVERAGE SURFACE ROUGHNESS, MAXIMUM PEAK HEIGHT, AND MAXIMUM PIT HEIGHT. RESPECTIVELY OBTAINED BY AFM MEASUREMENTS ON FOUR DIFFERENT AREAS

	S_a (μm)	S_p (μm)	S_v (μm)
"no ink"	0.126	0.186	-0.334
"ink1"	0.218	1.97	-1.52
"ink2"	0.148	0.978	-1.08
"ink3"	0.120	0.780	-1.23

the four measurements. S_a for the 3-D printed surface alone compares well with the results found in the state of the art [34]. Interestingly, S_a is on the same order also for the ink samples, and a limited variability is observed among the three measurements. Peaks and pits, which for the ink are mainly caused by solvent evaporation during curing steps, are lower than 2 μm in all cases.

Finally, the sheet resistance of the cured Ag ink is measured with the four-point probe method, and the result of 0.011 Ω/sq is obtained, independently of the linewidth, confirming the high-resolution potential of this approach, while ink thickness is about 10 μm for five-layer depositions.

III. ULTRAWIDEBAND 3-D CROSSOVER

The proposed manufacturing process is first applied to an ultrawideband 3-D crossover in microstrip technology. Such a circuit has been conceived to test the suitability of the manufacturing method to perform ink deposition on hardly accessible areas. Besides, crossovers are heavily utilized in MIMO front ends (see, for instance, the Butler matrix) and are, therefore, of interest for 5G.

The layout of the 3-D structure is shown in Fig. 7. The circuit is based on two 50-Ω lines crossing each other. The crossover consists of an overpass and an underpass obtained by cutting and bending the microstrip substrate. The radius of curvature is related to the dimension of the utilized brush. Indeed, the brush must access the interior of the node to realize both the ground plane of the overpassing line and the microstrip trace of the underpassing line. Utilizing a brush with a diameter of 4 mm, a radius of curvature of about 7–8 mm has been chosen. Besides, the edges in correspondence of the transition between straight and curved surfaces are blended to avoid the risk of reduced metal conductivity.

The manufactured prototype is illustrated in Fig. 8. Fig. 8(a) shows the photograph of an intermediate step (ink deposition), while the complete prototype is shown in Fig. 8(b). This circuit features limited parasitics (no vias) and eliminates the need for resonant components. Therefore, it can operate over extended frequency ranges, as required by next-generation communication systems. Besides, as the substrate at the exterior of the crossover is straight, the microstrip lines can be easily accessed with end-launch SMA connectors (connectors designed to operate up to 6 GHz are, here, utilized).

The circuit performance was tested with a FieldFox N9918A Vector Network Analyzer (VNA). Fig. 9 shows the S-parameters of the four-port circuit from 100 MHz to 5 GHz.
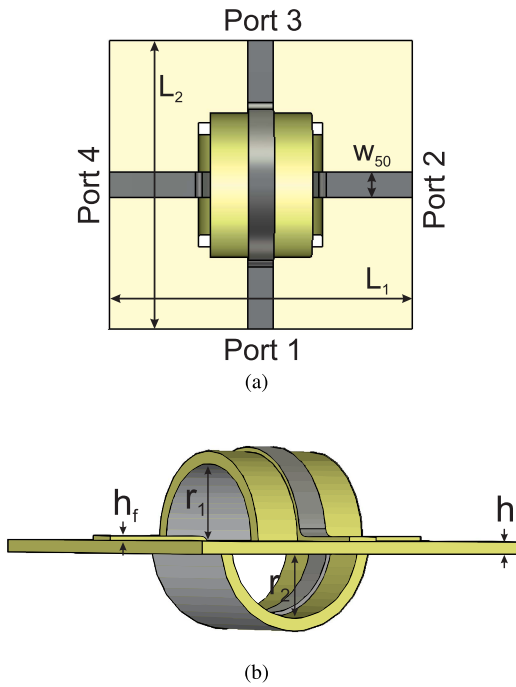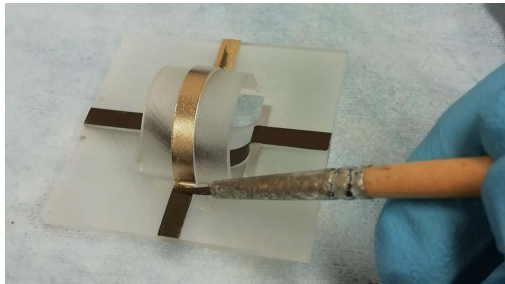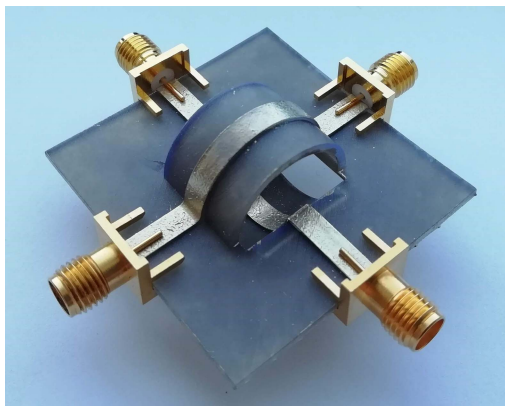
(a)

(b)

Fig. 7.   Layout of the ultrawideband 3-D crossover. (a) Top view. (b) Front view. Main circuit parameters: $L_1 = 42$ mm, $L_2 = 40$ mm, $w_{50} = 3.5$ mm, $r_1 = 8.6$ mm, $r_2 = 7.2$ mm, $h_f = 0.5$ mm, and $h = 1.4$ mm.

(a)

(b)

Fig. 8.   Fabricated prototype of the ultrawideband 3-D crossover. (a) Intermediate step. (b) Complete prototype.

The length of each line is about 50 mm, corresponding to an attenuation of −1.5 dB at 3.6 GHz [see Fig. 9(a)], with a maximum variability between the two lines lower than 0.3 dB, which can be due to manufacturing uncertainties and SMA connection variability. An isolation better than
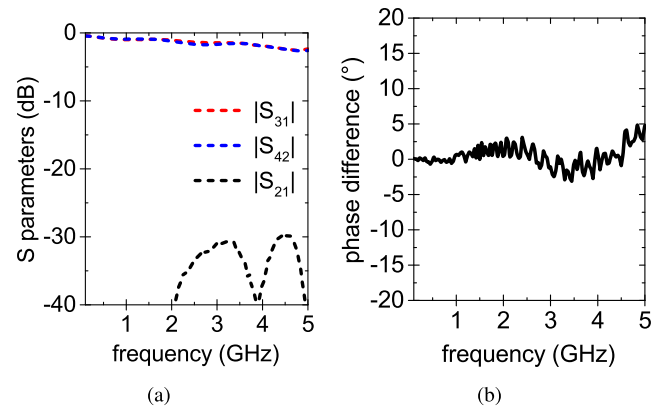

(a)   (b)

Fig. 9.   Measured S-parameters of the ultrawideband 3-D crossover. (a) Insertion loss and isolation of the two lines. (b) Phase difference.
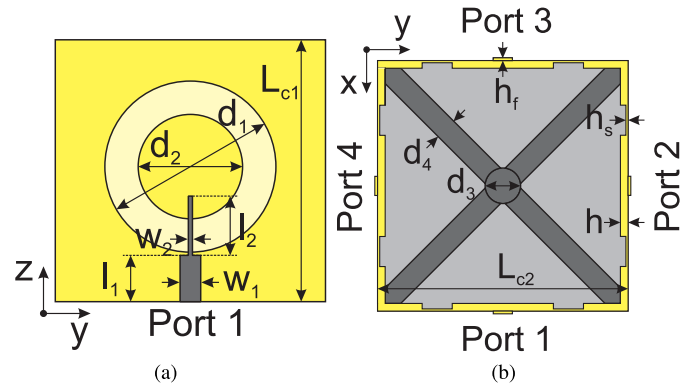

(a)   (b)

Fig. 10.   Layout of the MIMO antenna cube: (a) front view and (b) top view. Main circuit parameters: $d_1 = 29.1$ mm, $d_2 = 17.7$ mm, $l_1 = 7.85$ mm, $l_2 = 10.05$ mm, $w_1 = 3.5$ mm, $w_2 = 0.7$ mm, $h_f = 0.5$ mm, and $h_s = 0.4$ mm for the annular slot antenna; $L_{c1} = 44.4$ mm, $L_{c2} = 45.8$ mm, and $h = 1.4$ mm for the cube; and $d_3 = 6$ mm and $d_4 = 4$ mm for the internal structure of the cavity. Gray color is used for the metallized areas and yellow for the dielectric.

−30 dB is experienced throughout the whole band. The phase difference between the transmission coefficients of the two lines is lower than 5° for the whole considered band, as shown in Fig. 9(b), which confirms the ultrawideband operation of the crossover.

IV. MIMO ANTENNA TOPOLOGY

Finally, a 3-D antenna structure has been implemented. The 3-D printed antenna topology proposed in this paper consists of a cube, where four annular slot antennas, operating in the band 3.4–3.8 GHz, which is one of the sub-6-GHz bands destined for 5G applications in Europe [35], [36] (marked with a yellow box in all subsequent graphs), are placed on the lateral faces (one for each face), so that the proposed system has the capability to steer radiation over 360°. This antenna structure is thought for hotspot and access-point applications [37]. An additional structure is placed in the interior of the cube to decrease mutual coupling so that a good isolation level is achieved without requiring to make the antennas operate in orthogonal polarization.

A. Design Process

The main dimensions of the proposed antenna are reported in Fig. 10, including both the side view [see Fig. 10(a)] and the
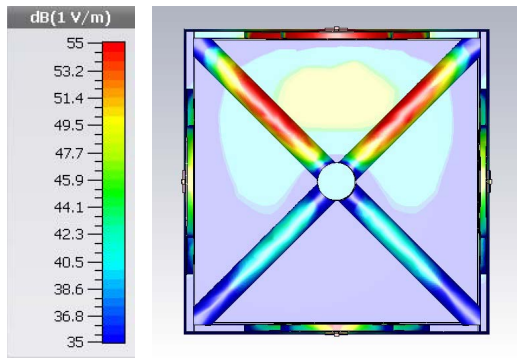
Fig. 11. Magnitude of the electric field distribution on the cross section of the cavity.

Fig. 12. Study of the impact of the post: S-parameters with and without the internal structure and as a function of the z-position of the horizontal cross (the offset is calculated with respect to the center of the cube). Dimensions are expressed in millimeters.

top view [see Fig. 10 (b)]. The antenna design is conducted within the CST environment. The slots are designed in the interior, while the proximity-coupled feedlines are placed on the exterior of the cube. The slot length is approximately equal to one guided wavelength at the central frequency of the band (i.e., 3.6 GHz), and the feedlines have been tuned to match the antennas to a 50-Ω impedance. Slot antennas are chosen for their low profile and their inherent capability to operate over broad bands (the antenna impedance bandwidth increases with the width of the slot [38]), whereas the resonant annular slot configuration is chosen instead of the rectangular slot because it guarantees higher gain and isolation between adjacent antennas. Moreover, being that the slotline is less sensitive than microstrip to dielectric losses, the slot antenna has been preferred in order to minimize the effect of the relatively high loss of the dielectric material.

The antenna is completed by a cross-shaped structure, placed in the internal volume of the cube to increase the isolation between the radiating elements. The structure is composed of a central vertical post and a horizontal cross.

The horizontal cross is placed in the middle of the cube to increase its decoupling effectiveness. The distance between the slots and the vertical post is approximately a quarter-wavelength at the central frequency, while the height and the width of the cube are equal to half-wavelength (the length of the sides of the cube corresponds to about $0.55\lambda_0$, where λ_0 is the free-space wavelength at 3.6 GHz). Both the cavity walls and the internal structure are covered with ink according to the procedure described in Section II.

Therefore, a resonant field is established in each triangular cavity obtained by intersecting the cube with two ideal half-planes delimited by the straight line passing through the center of the vertical post (parallel to the vertical post) and cross-cutting each of the two arms of the horizontal cross that separates each antenna from the adjacent ones. The electric field distribution on the plane perpendicular to the slots (xy plane), cutting the cube in the middle, is shown in Fig. 11. The front antenna [top side in Fig. 6(b)] is excited. A maximum of the E-field is noticed in the area close to the slot, whereas the field decreases approaching to the vertical post. The adoption of triangular cavities enables a considerable volume saving while maintaining a reduced coupling between antennas.
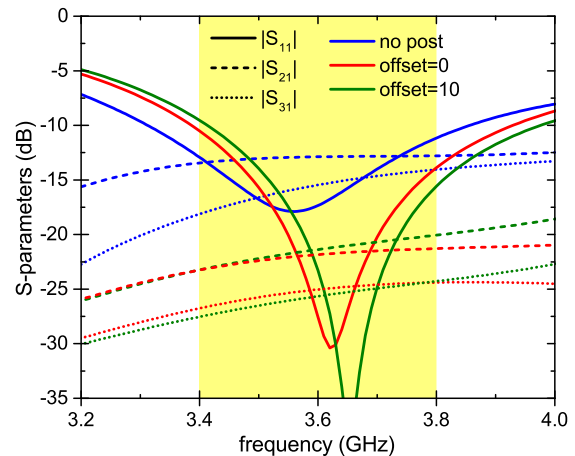
The impact of the cross-shaped structure is analyzed by reporting the relevant S-parameters of the proposed circuit (i.e., input reflection coefficient, $|S_{11}|$, and mutual coupling values between adjacent, $|S_{21}|$, and opposite-side, $|S_{31}|$, radiating elements), with and without the designed internal post, as shown in Fig. 12. Two different positions of the horizontal cross along the z-axis are also considered: "offset = 0" refers to the cross placed in the middle of the cube, while "offset = 10" indicates that the horizontal cross is translated by 10 mm along the z-axis. The analysis of the graph reveals that, when the internal structure is present with "offset = 0," $|S_{21}|$ decreases from -12.3 to -21.8 dB at the central frequency, while $|S_{31}|$ decreases from -17.1 to -25 dB. In addition, the horizontal cross attenuates $|S_{21}|$ more effectively when placed at "offset = 0," while $|S_{31}|$ is more attenuated in case "offset = 10." Since $|S_{21}|$ is the highest contribution, the case "offset = 0" is chosen for the present design.

A parametric study of the impact of the diameter of both the vertical post ($d3$) and the four horizontal axes ($d4$) on the S-parameters of the antenna topology is shown in Fig. 13. In Fig. 13(a), $d4$ is kept fixed to 4 mm, while $d3$ is varied. In Fig. 13(b), $d3$ is kept fixed to 6 mm, while $d4$ is varied. In both cases, the isolation among radiating elements improves as the diameters of the post and cross-shaped structure increase; at the same time, though, the resonant frequency is upshifted. Consequently, $d3 = 6$ mm and $d4 = 4$ mm are chosen as tradeoff values to guarantee a good isolation between elements without compromising in-band input matching. To get a higher isolation, not only $d3$ and $d4$ but also the cube sides must be increased.

B. Experimental Results and Discussion

Fig. 14 depicts the manufactured prototype at different stages. In Fig. 14(a), the antenna topology dielectric "scaffolding" is removed from the printer and cleaned off the excess liquid material. The structure at the base, made as well of clear material, represents the structural support, utilized by the
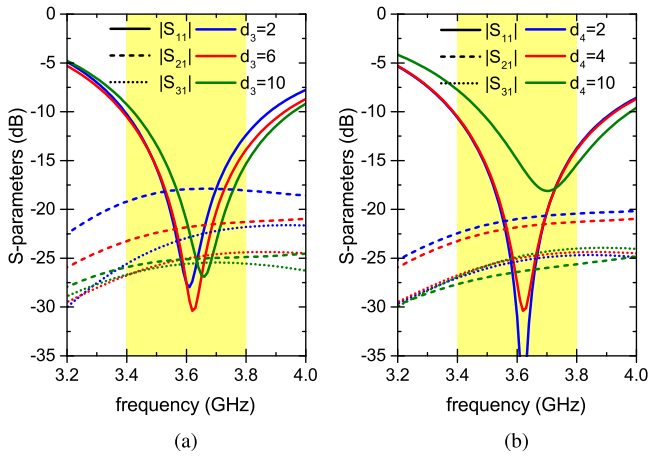
(a)   (b)

Fig. 13. Study of the impact of the dimension of the cross-shaped internal post on the S-parameters of the antenna topology. (a) S-parameters versus d_3. (b) S-parameters versus d_4. Dimensions are expressed in millimeters.

printer to put the object in a convenient orientation to optimize the printing process. The whole cube is fabricated as a single piece, including the interior cross-shaped structure, with the exception of the lid, which is separately manufactured. The removal of at least one of the top/bottom sides of the cube is needed to access the interior of the box and allow for selective metallization. Fig. 14(b) shows a detail of a metallized trace. Lines as thin as 0.7 mm are easily realized. Finally, Fig. 14(c) illustrates the completed prototype after metallization, including the lid. The complete cube weighs only 21.29 g. Four rectangular holes are present on the bottom of the cube so that each antenna is connected to an end-launch SMA connector (Fig. 15 shows the detail of the SMA-to-microstrip transition); metal epoxy is adopted for soldering. Therefore, the outer conductor of each connector is in contact with the ground plane in the interior of the cube, and all four SMAs are connected to the same ground potential, whereas their inner conductor is connected to the respective feedlines.

To realize this antenna structure with standard subtractive technologies, the following steps would be implemented: The four slots would be manufactured by using four dual-layer printed circuit boards, and the internal cross-shaped structure would be realized starting from five metal rods shaped with micromachining. Two additional metal panels would be utilized for the top and bottom lids, and the holes for the SMA connectors would be performed with drilling or laser machining. All these parts, realized with different manufacturing tools, would be soldered together, leading to a much more unstable, heavier, and expensive prototype and a high volume of material waste.

The MIMO antenna topology that is integrated on the 3-D printed cubic package is experimentally tested with a VNA. Leveraging the symmetry of the topology, the S-parameters referred to a single radiating element are considered, while the antennas not involved in the measurement are terminated with 50-Ω loads.

The input reflection coefficient is shown in Fig. 16(a). A good agreement between simulations and measurements is obtained. Minor variations are likely due to fabrication
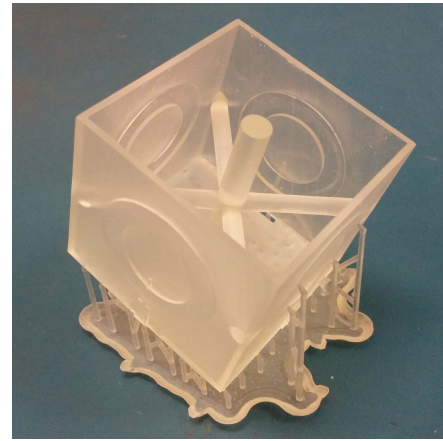
(a)
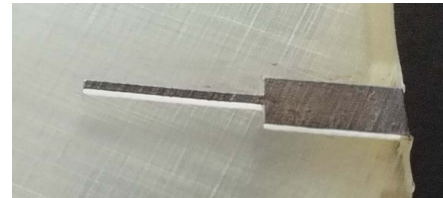
(b)

(c)

Fig. 14. Fabricated prototype of the MIMO antenna cube. (a) 3-D-printed circuit with support structure. (b) Detail of a metallized trace. (c) Complete prototype.

tolerances and to uncertainties in the EM properties of the sample caused by the additional curing steps. A downshift of the minimum $|S_{11}|$ of 65 MHz is experienced, which corresponds to 1.8% at the operating frequency. Nevertheless, the input reflection coefficient is below −10 dB in the whole band of interest. The measured impedance bandwidth of the antenna is about 16%.

Fig. 16(b) shows the mutual coupling between adjacent- and opposite-side-placed radiating elements. The coupling between adjacent elements reaches a maximum of −21 dB in the operating band, while the coupling between opposite antennas is lower than the expected value from simulations (about −30 dB). Both these values are quite good if compared with other MIMO systems based on copolarized antennas representing the state of the art.
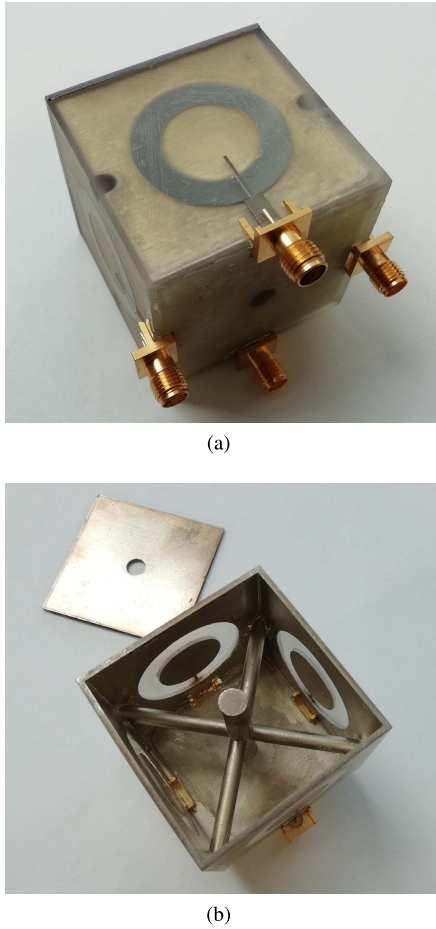
(a)

(b)

Fig. 15. Detail of the SMA-to-microstrip connection for antenna testing: (a) exterior and (b) interior of the cube.
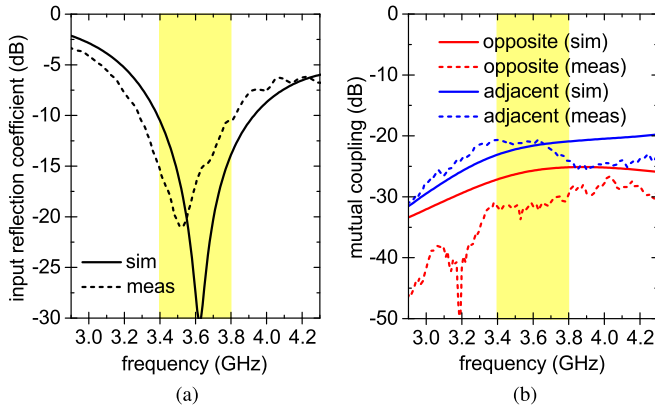

Fig. 16. Simulated and measured S-parameters of the proposed MIMO antenna topology: (a) input reflection coefficient, $|S_{11}|$, and (b) mutual coupling between opposite, $|S_{31}|$ (red curve), and adjacent, $|S_{21}|$ (blue curve), antennas.

The simulated and measured radiation patterns of a single antenna are depicted in Fig. 17. The measurements are taken in an environment with anechoic provisions. The radiation patterns are evaluated at 3.6 GHz for both the xy (H-plane) and the xz (E-plane) cuts. As expected, the antenna is linearly polarized with a cross-polar component at least 22 dB below the copolar. The maximum of the radiated field occurs in broadside direction, and the radiation patterns are unidirectional, with a front-to-back ratio of 10 dB.
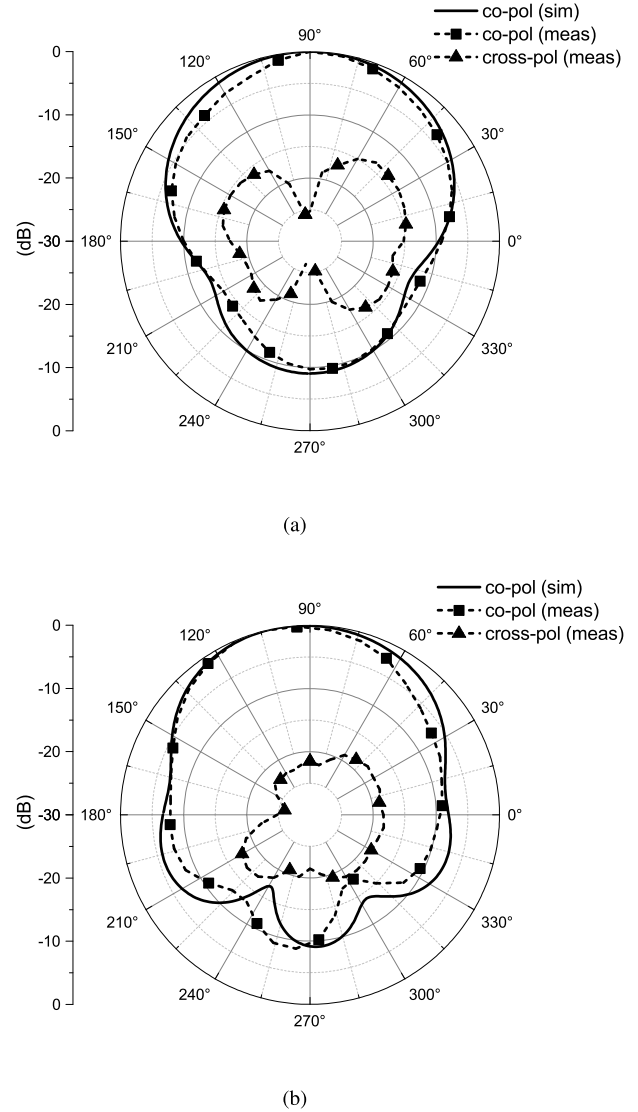

(a)

(b)

Fig. 17. Simulated and measured radiation patterns when one radiating element is excited: (a) xy (H- or ϕ-) plane and (b) xz (E- or θ-) plane.

The half-power beamwidth is about $101°$ in the H-plane and $81°$ in the E-plane.

The gain of a single radiating element, evaluated in broadside direction, is reported as well (see Fig. 18). In the band of interest, the measured gain varies between 3.6 and 5.1 dBi, in good agreement with the simulation results, corresponding to radiation efficiencies in the range [65–92]%. It is worth noticing that the antenna gain takes on values around 5 dBi also outside the band of interest, between 3.8 and 4.4 GHz.

Finally, an evaluation of the proposed antenna topology in terms of channel diversity reception is performed. An essential criterion to assess the behavior of an MIMO system is the envelope correlation coefficient (ECC). From [39], the ECC between any two antennas (denoted by i and j) in an MIMO system consisting of N antennas [$\rho_e(i, j, N)$] can be derived from their radiation patterns as follows:

$$\rho_e(i, j, N) = \frac{\left| \iint_{4\pi} E_i(\theta, \phi) \cdot E_j^*(\theta, \phi) \, d\Omega \right|^2}{\iint_{4\pi} |E_i(\theta, \phi)|^2 \, d\Omega \cdot \iint_{4\pi} |E_j(\theta, \phi)|^2 \, d\Omega} \quad (1)$$

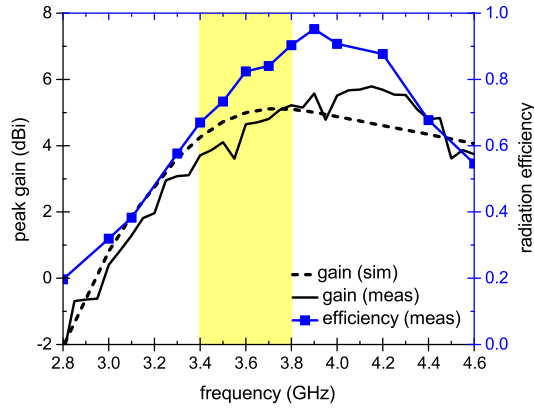where $E_i(\theta, \phi)$ is the electric field radiated by ith antenna.

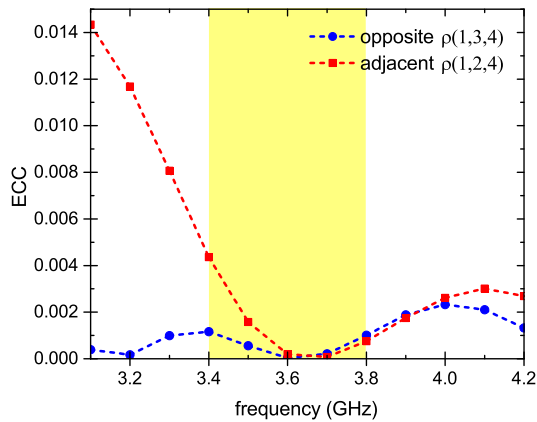Fig. 18. Peak gain and radiation efficiency of a single radiating element.

Fig. 19. ECC of the proposed MIMO antenna topology. The correlation between opposite-side placed (blue curve) and adjacent (red curve) slots is reported.

In the present case, $N = 4$ and, given the symmetry of the topology, the performance can be evaluated by considering only two correlation parameters, namely, ECC between adjacent antennas [$\rho_e(1, 2, 4)$] and ECC between opposite-side placed antennas [$\rho_e(1, 3, 4)$]. Fig. 19 illustrates the values of ECC derived from antenna-simulated radiation patterns in CST. The ECC is lower than 0.005 in all bands, well below the acceptable limit of 0.5 [39], thus testifying the excellent capability of the proposed MIMO system to take advantage of channel diversity.

Likewise, an important parameter to characterize the radiation performance of a multiport antenna system is the total active reflection coefficient (TARC) [15]. It is defined as the ratio of the square root of the total reflected power divided by the square root of the total incident power, and for an N-port system, it can be expressed as

$$\Gamma_a^t = \sqrt{\sum_{i=1}^{N} |b_i|^2} \Big/ \sqrt{\sum_{i=1}^{N} |a_i|^2} \qquad (2)$$

where a_i is the incident signal at each port and b_i is the reflected signal at each port. Since the incident and reflected signals are related to the S-matrix as follows:
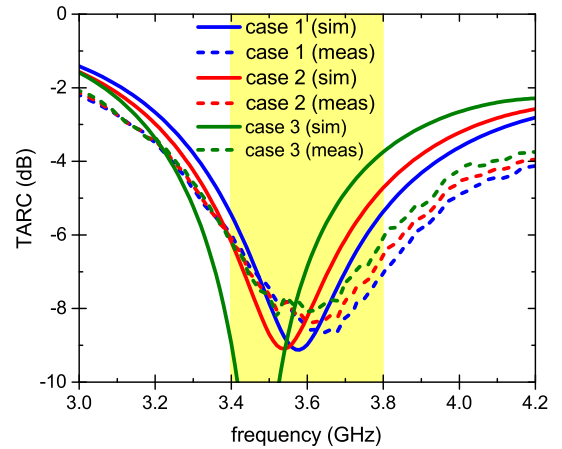
$$b = \mathbf{S}a \qquad (3)$$

Fig. 20. TARC of the proposed MIMO antenna for three different excitations: one element is excited ("case 1"), two elements are excited in phase ("case 2"), and four elements excited in phase ("case 3").

TARC can be evaluated on the basis of the S-parameters. In particular, according to both the property of reciprocity of the antennas and the symmetry of the proposed topology, $S_{21} = S_{12} = S_{32} = S_{23} = S_{34} = S_{43} = S_{41} = S_{14}$ and $S_{31} = S_{13} = S_{42} = S_{24}$. As a consequence, the TARC can be determined on the basis of only three S-parameters, namely, S_{11}, S_{12}, and S_{13}.

Three excitation cases have been considered in this paper. First, only the first port is excited, whereas all the other ports are connected to matched loads (i.e., $a_1 = 1$ and $a_2 = a_3 = a_4 = 0$). As a consequence, (2) becomes as follows:

$$\Gamma_{a1}^t = \sqrt{\sum_{j=1}^{4} |S_{1j}|^2} = \sqrt{|S_{11}|^2 + 2|S_{12}|^2 + |S_{13}|^2} \qquad (4)$$

the latter equality being due to the symmetry of the structure. In the second case, adjacent elements (both ports 1 and 2) are excited in phase (i.e., $a_1 = a_2 = 1/\sqrt{2}$ and $a_3 = a_4 = 0$). Again, the following expression is obtained by exploiting the symmetry of the topology:

$$\Gamma_{a2}^t = \sqrt{|S_{11} + S_{12}|^2 + |S_{12} + S_{13}|^2}. \qquad (5)$$

Finally, all elements are excited in phase (i.e., $a_1 = a_2 = a_3 = a_4 = 1/2$). This corresponds to

$$\Gamma_{a3}^t = \sqrt{|S_{11} + 2S_{12} + S_{13}|^2}. \qquad (6)$$

The results are illustrated in Fig. 20. A satisfactory -6-dB bandwidth of about 410 MHz (including the band of interest) is measured in all excitation cases.

The proposed MIMO antenna has also interesting beam-steering properties. In fact, feeding each slot individually, four radiation patterns can be obtained, rotated by 90° with respect to the neighbors, as depicted in Fig. 21(a). In addition, when a couple of adjacent antennas are fed in phase [10], the maximum of the resulting radiation pattern lies in between the maxima of the original radiation patterns of the two antennas, as anticipated in [40] and shown in Fig. 21(b). As an aggregate, in case the antenna topology is fed through the network proposed in [40], all of the xy plane is uniformly covered, and eight steerable directions can be obtained from
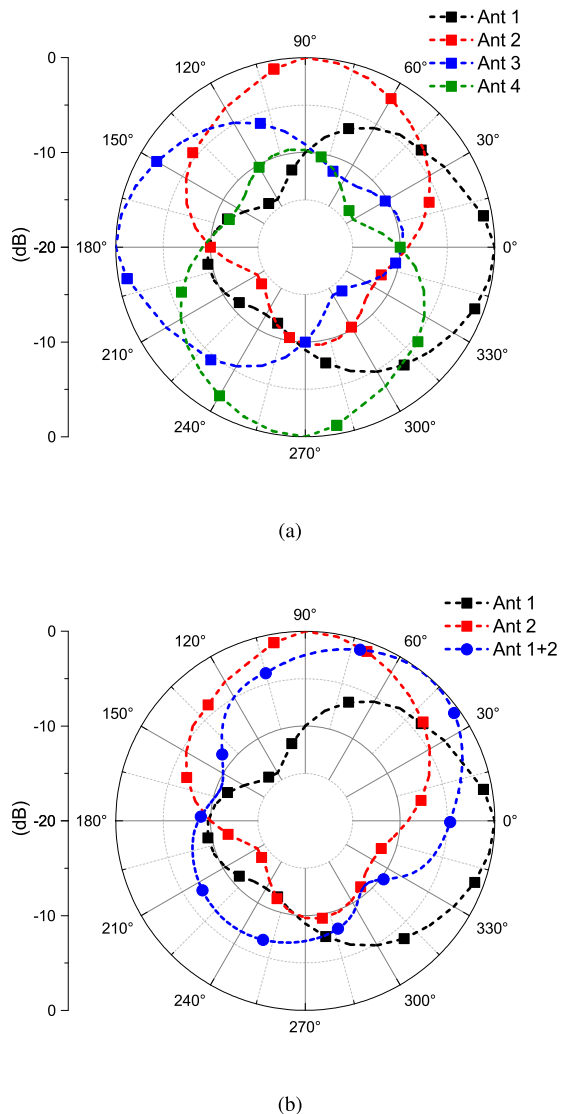
(a)

Fig. 21. Radiation patterns on the xy plane (H-plane cut). (a) All slot antennas fed one at a time and (b) antennas 1 and 2 both individually and jointly fed.
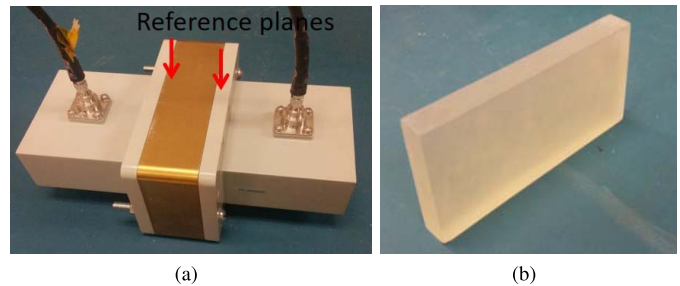

Fig. 22. Characterization of clear material: (a) setup and (b) sample under test.

the adopted 3-D printing technology, the whole system, consisting of a cube with four slot radiating elements, has been fabricated as a single block plus the lid. By taking advantage of a fully printed cross-shaped metal-coated structure in the interior of the cube, high isolation between the radiation elements is achieved (i.e., mutual coupling lower than −21 dB between adjacent and −32 dB between opposite-side placed elements). The good agreement between simulations and measurements testifies the accuracy of the electromagnetic characterization of the adopted 3-D printed material and the consistency of the printing process. In the end, an ECC lower than 0.005 and a TARC lower than −6 dB are obtained throughout the whole band, meaning that the system is thoroughly suited to effectively exploit channel diversity.

V. Conclusion

A novel manufacturing technology, aimed at achieving high-resolution ink patterns on complex 3-D antennas, packaging, and microwave structures, has been presented. By conveniently either embossing or engraving suitable areas of the prototype, selective metallization with silver nanoparticle ink has been achieved, with both high accuracy (metal traces as thin as 135 μm have been realized), low sheet resistance (0.011 Ω/sq), and low surface roughness ($S_a < 0.220$ μm). The process has been first successfully applied to a 3-D crossover tested in the band 100 MHz–5 GHz and finally applied to an MIMO antenna topology working in the band 3.4–3.8 GHz. Thanks to

four radiating elements, thus proving the capability of the system to provide high angle diversity [8] and its suitability for diverse applications, such as, for instance, hotspot and access-point implementations.

Appendix

The characterization of the 3-D printed "clear" resin from Formlab is performed by using a WR340 waveguide [see Fig. 22(a)]. Its unimodality band lies in the range 2.2–3.3 GHz, which is within the working band of the crossover and close to the operating band of the antenna (i.e., 3.4–3.8 GHz). Therefore, the obtained results can be considered valid with a good approximation for the designs presented in this paper.

The proposed method can be considered an alternative to other characterization methods suitable for microwave frequencies, such as Nicholson–Ross–Weir (NRW) [41]. The waveguide is connected to a VNA, and a calibration is performed, so that the reference planes of the measured S-parameters are set at the borders of a 3.6-cm-thick spacer [the brown component in Fig. 22(a)]. The advantage of the proposed technique is that it does not require that the sample has the same thickness as the available sampler, thus avoiding the problem of singularities at frequencies corresponding to an electrical length of $\lambda/2$ [32]. Indeed, two samples of clear material, with the same cross section as the spacer and variable thickness (i.e., 1.04 and 2.02 cm, respectively), are fabricated [in Fig. 22(b), one of the samples is reported]. The first one is referred to as "sample1," the second one as "sample2." Two samples are considered instead of one to compensate for possible uncertainties in the block dimension stemming from fabrication tolerances. Moreover, two samples are also useful to verify the consistency of the electromagnetic properties between one sample and the other. Then, the aforementioned geometries are electromagnetically simulated with the CST
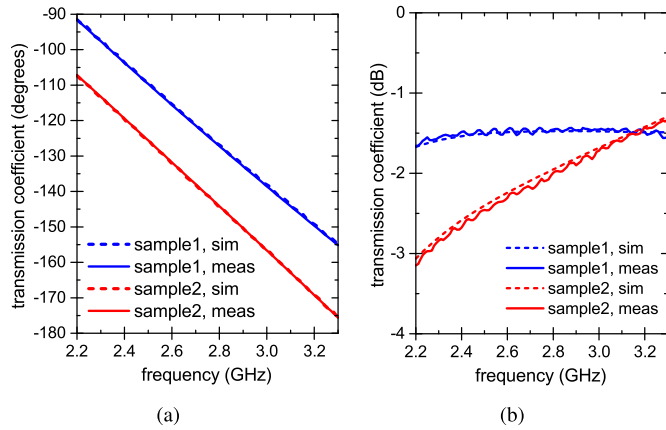
Fig. 23. Characterization of clear material. (a) Phase and (b) magnitude in dB of the transmission coefficient of the waveguide, loaded with the samples of clear material under test.
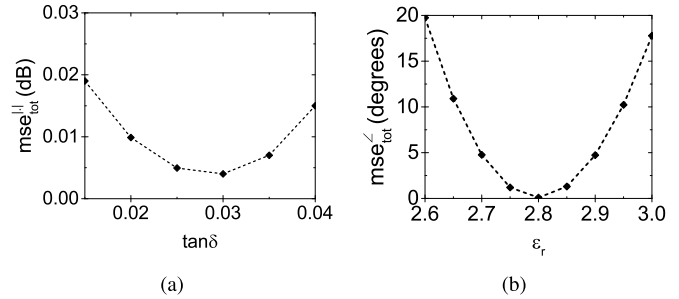

Fig. 24. Characterization of clear material: (a) total mse for the magnitude and (b) total mse for the phase of the transmission coefficient.

Microwave Studio, and both permittivity ϵ_r and dielectric loss $\tan\delta$ of the samples are varied so as to achieve a good matching between simulations and measurements for both blocks. In particular, the permittivity is used to obtain an agreement between the phases of the transmission coefficients over frequency (i.e., $\angle S_{21}$), while the dielectric loss is used for the matching of the magnitude of the transmission coefficients (i.e., $dB|S_{21}|$).

Fig. 23 shows a comparison between simulations and measurements of the transmission coefficient of the waveguide, loaded with one sample of clear material at a time. The permittivity is varied in steps of 0.05, and the chosen ϵ_r is the one, which minimizes the sum of the mean square error (mse) for the phase of the transmission coefficient ($\mathrm{mse}_{\mathrm{tot}}^{\angle}$) for the two samples, i.e., $\mathrm{mse}_{s1}^{\angle}$ and $\mathrm{mse}_{s2}^{\angle}$, calculated as follows:

$$\epsilon_{r,\mathrm{opt}} = \arg\min_{\epsilon_r} \mathrm{mse}_{\mathrm{tot}}^{\angle}$$
$$= \arg\min_{\epsilon_r} \left(\mathrm{mse}_{s1}^{\angle} + \mathrm{mse}_{s2}^{\angle}\right). \qquad (7)$$

Each term $\mathrm{mse}_{s\ i}^{\angle}$ is evaluated as follows:

$$\mathrm{mse}_{s\ i}^{\angle} = \frac{\sum_{k=1}^{N}(\angle S_{21}(f_k)_{\mathrm{sim}\ i} - \angle S_{21}(f_k)_{\mathrm{meas}\ i})^2}{N} \qquad (8)$$

where N is the number of frequency points, where the S-parameters are evaluated.

Same procedure is repeated for the dielectric loss

$$\tan\delta_{\mathrm{opt}} = \arg\min_{\tan\delta} \mathrm{mse}_{\mathrm{tot}}^{|\cdot|}$$
$$= \arg\min_{\tan\delta} \left(\mathrm{mse}_{s1}^{|\cdot|} + \mathrm{mse}_{s2}^{|\cdot|}\right). \qquad (9)$$

where each term $\mathrm{mse}_{s\ i}^{|\cdot|}$ is obtained as follows:

$$\mathrm{mse}_{s\ i}^{|\cdot|} = \frac{\sum_{k=1}^{N}(dB|S_{21}(f_k)|_{\mathrm{sim}\ i} - dB|S_{21}(f_k)|_{\mathrm{meas}\ i})^2}{N}. \qquad (10)$$

In the latter case, $\tan\delta$ is varied in steps of 0.005.

Fig. 24 illustrates both $\mathrm{mse}_{\mathrm{tot}}^{\angle}$ [see Fig. 24(a)] as a function of permittivity and $\mathrm{mse}_{\mathrm{tot}}^{|\cdot|}$ [see Fig. 24(b)] as a function of

dielectric loss. In the optimum case, corresponding to an $\epsilon_{r,\mathrm{opt}} = 2.8$ and $\tan\delta = 0.03$, $\mathrm{mse}_{\mathrm{tot}}^{\angle} = 0.091°$ and $\mathrm{mse}_{\mathrm{tot}}^{|\cdot|} = 0.004$ dB.

REFERENCES

[1] M. R. Palattella *et al.*, "Internet of Things in the 5G era: Enablers, architecture, and business models," *IEEE J. Sel. Areas Commun.*, vol. 34, no. 3, pp. 510–527, Mar. 2016.

[2] *Spectrum Frontiers: The New World of Millimeter-Wave Mobile Communication*, Federal Communications Commission, Washington, D.C., USA, Mar. 2016.

[3] A. Syed Nauroze *et al.*, "Additively manufactured RF components and modules: Toward empowering the birth of cost-efficient dense and ubiquitous IoT implementations," *Proc. IEEE*, vol. 105, no. 4, pp. 702–722, Apr. 2017.

[4] L. Roselli *et al.*, "Smart surfaces: Large area electronics systems for Internet of Things enabled by energy harvesting," *Proc. IEEE*, vol. 102, no. 11, pp. 1723–1746, Nov. 2014.

[5] F. Alimenti *et al.*, "Smart hardware for smart objects: Microwave electronic circuits to make objects smart," *IEEE Microw. Mag.*, vol. 19, no. 6, pp. 48–68, Sep./Oct. 2018.

[6] S. Schwarz and M. Rupp, "Exploring coordinated multipoint beamforming strategies for 5G cellular," *IEEE Access*, vol. 2, pp. 930–946, 2014.

[7] P. Roblin, M. Rawat, and V. Ratnasamy, "RF front-end flexibility, self-calibration, and self-linearization: Characterizing and mitigating nonlinearities in SDR MIMO systems for concurrent multiband operation," *IEEE Microw. Mag.*, vol. 19, no. 2, pp. 49–61, Mar./Apr. 2018.

[8] Z. N. Chen, D. Liu, H. Nakano, X. Qing, and T. Zwick, *Handbook of Antenna Technologies*. Singapore: Springer, 2016.

[9] F. C. Robey, S. Coutts, D. Weikle, J. C. McHarg, and K. Cuomo, "MIMO radar theory and experimental results," in *Proc. Conf. Rec. 38th Asilomar Conf. Signals, Syst. Comput.*, vol. 1, Nov. 2004, pp. 300–304.

[10] S. Sun, T. S. Rappaport, R. W. Heath, Jr., A. Nix, and S. Rangan, "MIMO for millimeter-wave wireless communications: Beamforming, spatial multiplexing, or both?" *IEEE Commun. Mag.*, vol. 52, no. 12, pp. 110–121, Dec. 2014.

[11] S. H. Chae, S.-K. Oh, and S.-O. Park, "Analysis of mutual coupling, correlations, and TARC in WiBro MIMO array antenna," *IEEE Antennas Wireless Propag. Lett.*, vol. 6, pp. 122–125, 2007.

[12] M. S. Sharawi, M. U. Khan, A. B. Numan, and D. N. Aloi, "A CSRR loaded MIMO antenna system for ISM band operation," *IEEE Trans. Antennas Propag.*, vol. 61, no. 8, pp. 4265–4274, Aug. 2013.

[13] G. Srivastava and A. Mohan, "Compact MIMO slot antenna for UWB applications," *IEEE Antennas Wireless Propag. Lett.*, vol. 15, pp. 1057–1060, 2016.

[14] Y. K. Choukiker, S. K. Sharma, and S. K. Behera, "Hybrid fractal shape planar monopole antenna covering multiband wireless communications with MIMO implementation for handheld mobile devices," *IEEE Trans. Antennas Propag.*, vol. 62, no. 3, pp. 1483–1488, Mar. 2014.

[15] M. Manteghi and Y. Rahmat-Samii, "Multiport characteristics of a wide-band cavity backed annular patch antenna for multipolarization operations," *IEEE Trans. Antennas Propag.*, vol. 53, no. 1, pp. 466–474, Jan. 2005.

[16] B. N. Getu and J. B. Andersen, "The MIMO cube—A compact MIMO antenna," *IEEE Trans. Wireless Commun.*, vol. 4, no. 3, pp. 1136–1141, May 2005.

[17] W. Han, X. Zhou, J. Ouyang, Y. Li, R. Long, and F. Yang, "A six-port MIMO antenna system with high isolation for 5-GHz WLAN access points," *IEEE Antennas Wireless Propag. Lett.*, vol. 13, pp. 880–883, 2014.

[18] S. Sheel and J. C. Coetzee, "A compact dielectric-filled slotted cavity MIMO antenna," *Prog. Electromagn. Res. Lett.*, vol. 72, pp. 17–22, Jan. 2018.

[19] J.-B. Yan, C.-Y. Chiu, and R. D. Murch, "24-Port and 36-port antenna cubes suitable for MIMO wireless communications," *IEEE Trans Antennas Propag.*, vol. 56, no. 4, pp. 1170–1176, Apr. 2008.

[20] A. Jain, P. Verma, and V. K. Singh, "PIFA-based 16×20 large MIMO cube antenna," *Microw. Opt. Technol. Lett.*, vol. 57, no. 3, pp. 685–690, Mar. 2015.

[21] Y. Pan, Y. Cui, and R. Li, "Investigation of a triple-band multibeam MIMO antenna for wireless access points," *IEEE Trans. Antennas Propag.*, vol. 64, no. 4, pp. 1234–1241, Apr. 2016.

[22] J. Zheng, X. Gao, Z. Zhang, and Z. Feng, "A compact eighteen-port antenna cube for MIMO systems," *IEEE Trans Antennas Propag.*, vol. 60, no. 2, pp. 445–455, Feb. 2012.

[23] G.-L. Huang, S.-G. Zhou, and T. Yuan, "Development of a wideband and high-efficiency waveguide-based compact antenna radiator with binder-jetting technique," *IEEE Trans. Compon., Packag., Manuf. Technol.*, vol. 7, no. 2, pp. 254–260, Feb. 2017.

[24] B. Zhang *et al.*, "Metallic 3-D printed antennas for millimeter- and submillimeter wave applications," *IEEE Trans. THz Sci. Technol.*, vol. 6, no. 4, pp. 592–600, Jul. 2016.

[25] G. Dias, P. Pinho, R. Gonçalves, and N. Carvalho, "3D antenna for wireless power transmission: Aperture coupled microstrip antenna with dielectric lens," in *Proc. IEEE Int. Appl. Comput. Electromagn. Soc. Symp.-Italy (ACES)*, Mar. 2017, pp. 1–2.

[26] R. A. Bahr, Y. Fang, W. Su, B. Tehrani, V. Palazzi, and M. M. Tentzeris, "Novel uniquely 3D printed intricate Voronoi and fractal 3D antennas," in *IEEE MTT-S Int. Microw. Symp. Dig.*, Jun. 2017, pp. 1583–1586.

[27] V. Palazzi *et al.*, "A novel additive-manufactured multiple-infill ultra-lightweight cavity-backed slot antenna for UWB applications," in *Proc. 47th Eur. Microw. Conf. (EuMC)*, Oct. 2017, pp. 252–255.

[28] J. Kimionis, M. Isakov, B. S. Koh, A. Georgiadis, and M. M. Tentzeris, "3D-printed origami packaging with inkjet-printed antennas for RF harvesting sensors," *IEEE Trans. Microw. Theory Techn.*, vol. 63, no. 12, pp. 4521–4532, Dec. 2015.

[29] R. A. Ramirez, M. Golmohamadi, J. Frolik, and T. M. Weller, "3D printed on-package tripolar antennas for mitigating harsh channel conditions," in *Proc. IEEE Radio Wireless Symp. (RWS)*, Jan. 2017, pp. 62–64.

[30] W. Su, R. Bahr, S. A. Nauroze, and M. M. Tentzeris, "3D printed reconfigurable helical antenna based on microfluidics and liquid metal alloy," in *Proc. IEEE Int. Symp. Antennas Propag. (APSURSI)*, Jun./Jul. 2016, pp. 469–470.

[31] *Form 2*. Accessed: Jun. 9, 2019. [Online]. Available: https://formlabs.com/3d-printers/form-2/

[32] P. I. Deffenbaugh, R. C. Rumpf, and K. H. Church, "Broadband microwave frequency characterization of 3-D printed materials," *IEEE Trans. Compon., Packag., Manuf. Technol.*, vol. 3, no. 12, pp. 2147–2155, Dec. 2013.

[33] Zeiss. *SV 6 and SV 11 Stereomicroscopes—Operating Instructions*. Accessed: Jun. 9, 2019. [Online]. Available: http://files.lordil.fr/manuel-utilisation-sv6-et-sv11-carl-zeiss.pdf

[34] J. Maas, B. Liu, S. Hajela, Y. Huang, X. Gong, and W. J. Chappell, "Laser-based layer-by-layer polymer stereolithography for high-frequency applications," *Proc. IEEE*, vol. 105, no. 4, pp. 645–654, Apr. 2017.

[35] S. Apicella. (Jul. 2018). 5G Deployment Strategies for Europe. ITU Seminar: 5G Implementation in Europe and CIS. [Online]. Available: https://www.itu.int/en/ITU-D/Regional-Presence/Europe/Documents/Events/2018/5GHungary/S2%20Sylvana%20Apicella%20Possible%205G%20Deployment%20for%0Europe%20Rev.A%20External.pdf

[36] Qualcomm Technologies. (Dec. 2017). *Spectrum for 4G and 5G*. [Online]. Available: https://www.qualcomm.com/media/documents/files/spectrum-for-4g-and-5g.pdf

[37] Ericsson, Stockholm, Sweden. *Ericsson Mobility Report*. Accessed: Nov. 2018. [Online]. Available: https://www.ericsson.com/assets/local/mobility-report/documents/2018/ericsson-mobility-report-november-2018.pdf

[38] J.-S. Row, W.-L. Liu, and T.-R. Chen, "Circular polarization and polarization reconfigurable designs for annular slot antennas," *IEEE Trans. Antennas Propag.*, vol. 60, no. 12, pp. 5998–6002, Dec. 2012.

[39] R. G. Vaughan and J. B. Andersen, "Antenna diversity in mobile communications," *IEEE Trans. Veh. Technol.*, vol. VT-36, no. 4, pp. 149–172, Nov. 1987.

[40] V. Palazzi, P. Mezzanotte, and L. Roselli, "A novel agile phase-controlled beamforming network intended for 360° angular scanning in MIMO applications," in *IEEE MTT-S Int. Microw. Symp. Dig.*, Jun. 2018, pp. 1–4.

[41] W. B. Weir, "Automatic measurement of complex dielectric constant and permeability at microwave frequencies," *Proc. IEEE*, vol. 62, no. 1, pp. 33–36, Jan. 1974.

Valentina Palazzi (S'15–M'19) received the B.Sc. and M.Sc. degrees *(magna cum laude)* in electronic engineering and the Ph.D. degree in industrial and information engineering from the University of Perugia, Perugia, Italy, in 2012, 2014, and 2018, respectively.

In 2015, she was a Visiting Ph.D. Student with the Tyndall National Institute, Cork, Ireland. In 2016, she visited the Center Tecnològic de Telecomunicacions de Catalunya, Barcelona, Spain, sponsored by the COST Action IC1301 Wireless Power Transmission for Sustainable Electronics. In 2016, she joined the Agile Technologies for High-Performance Electromagnetic Novel Applications Research Group, School of Electrical and Computer Engineering, Georgia Institute of Technology, Atlanta, GA, USA, where she was involved in additive manufacturing technologies and flexible electronics. She is currently a Researcher with the High Frequency Electronics Laboratory, University of Perugia. Her current research interests include the design of passive transponders with sensing capabilities, radar front ends, wireless power transfer technologies, additive manufacturing processes, and conformal electronics.

Dr. Palazzi is a member of IEEE MTT-S TC-24 RFID Technologies. She was a recipient of the First Place Award of the IEEE MTT-S Student Design Competition on Wireless Energy Harvesting held at the International Microwave Symposium 2016. She was also a recipient of the IEEE MTT-S Graduate Fellowship in 2017 and the 2017 MTT-S Prize Italy Chapter Central and Southern Italy.

Wenjing Su (S'14–M'18) received the B.S. degree in electrical engineering from the Beijing Institute of Technology, Beijing, China, in 2013, and the Ph.D. degree in electrical and computer engineering from the Georgia Institute of Technology, Atlanta, GA, USA, in 2018.

In Fall 2013, she joined the Agile Technologies for High-Performance Electromagnetic Novel Applications (ATHENA) Research Group, Georgia Institute of Technology, led by Dr. M. M. Tentzeris. She is currently with Google, Mountain View, CA, USA. She has authored over 34 papers in refereed journals and conference proceedings. She holds four patents/patent applications. Her research interfaces advance novel fabrication technique (e.g., inkjet printing and 3-D printing), special mechanical structures (e.g., microfluidics and origami), microwave components/antennas to solve problems in smart health, and wearable electronics in Internet-of-Things (IoT) applications. Her current research interests include wearable antennas, flexible electronics, applied electromagnetics, additively manufactured electronics, wireless sensing, machine-learning aid sensing, green electronics, RFID, and reconfigurable antennas.

Ryan Bahr (S'14) received the B.S. degree *(summa cum laude)* with a focus on RF engineering and the M.S. degree with a focus on electromagnetics and a minor in computer science from the Georgia Institute of Technology, Atlanta, GA, USA, in 2013 and 2015, respectively.

He is currently a Research Assistant with the ATHENA Research Laboratory, Georgia Institute of Technology, where he focuses on the development of 3-D electromagnetic designs utilizing additive manufacturing. He designs complex electromagnetic structures with additive manufacturing utilizing technologies, such as fused deposition modeling, stereolithography, and inkjet printing. He is involved in mathematically inspired structures, inkjet printing of flexible electronics, and the utilization of additive manufacturing for RF packaging and millimeter-wave electronics.

Mr. Bahr was a recipient of the Best Student Poster Award of Gomac Tech 2016 for additively manufactured flexible and origami-reconfigurable RF sensors and the Flex2018 Best Poster for additive manufacturing of mmWave designs for flexible hybrid electronics (FHE).

Silvia Bittolo-Bon received the master's degree in materials engineering and the Ph.D. degree in materials nanotechnology from the University of Perugia, Perugia, Italy, in 2003 and 2008, respectively.

She currently holds a contract for research with the National Consortium of Materials Science (INSTM), Civil and Environmental Engineering Department, University of Perugia, where she focuses on the development of bioinspired materials. She designs complex material architectures for bionicomposites. She is also involved in research activities in the field of the development and characterization of nanostructured multifunctional hybrid materials. She is the author of 42 publications in international journals with citation index (15 as h-index and 942 citations in Scopus).

Federico Alimenti (S'91–A'97–M'06–SM'09) received the Laurea degree *(magna cum laude)* and the Ph.D. degree in electronic engineering from the University of Perugia, Perugia, Italy, in 1993 and 1997, respectively.

In 1996, he was a Visiting Scientist with the Technical University of Munich, Munich, Germany. Since 2001, he has been with the Department of Engineering, University of Perugia, where he has been involved in teaching the class of microwave electronics. From 2011 to 2014, he was the Scientific Coordinator of the ENIAC ARTEMOS Project. In 2014, he was a Visiting Professor with EPFL, Lausanne, Switzerland. In 2018, he got the qualification as a Full Professor and received the Mario Sannino Award for the best research in the field of microwave electronics. He has authored a European patent (EP2660755) and more than 170 papers in journals and conferences. His h-index is 20 with more than 1300 citations (Source: Scopus) and 22 with more than 1800 citations (source: Google Scholar). His current research interests include microwave circuit design.

Dr. Alimenti was a recipient of the URSI Young Scientist Award by the Technical University of Munich in 1996. In 2013, he was the recipient of the IET Premium (Best Paper) Award and the TPC Chair of the IEEE Wireless Power Transfer Conference. He has participated at the Summer School 2017, held at Infineon Austria AG, Villach, Austria, as a Keynote Lecturer.

Paolo Mezzanotte (M'12) was born in Perugia, Italy, in 1965. He received the Ph.D. degree from the University of Perugia, Perugia, in 1997.

Since 2007, he has been an Associate Professor with the University of Perugia, where he has been involved in teaching the classes of radio frequencies engineering and systems and circuits for the Internet of Things (IoT). Since 2014, he has been the Vice Head of the Department of Engineering, University of Perugia. His current h-index is 24. His current research interests include the development of microwave circuits on biocompatible substrates and the enabling technologies for IoT. These research activities are testified by over 170 publications in the most reputed specialized journals and at the main conferences of the microwave scientific community.

Dr. Mezzanotte is also the Chair of the IEEE Technical Committee MTT-24-RFID Technologies. He is also an Associate Editor of the *Applied Computational Electromagnetics Society Journal*.

Luca Valentini received the master's degree in physics from the University of Perugia, Perugia, Italy, and the Ph.D. degree in materials science from the University of Naples Federico II, Naples, Italy, in 2001.

He is currently an Associate Professor of materials science and technology with the University of Perugia. He is the author of more than 160 publications in international journals with citation index (39 as h-index and 5680 citations in Scopus) and several publications in international conferences in the fields of materials science, polymer physics, and bionic composites.

Dr. Valentini is also a member of the Graphene Flagship WorkPackage 14 Polymer Composites. He is also an Associate Editor of polymer and composite materials topic for the journal *Frontiers in Materials*.

Manos M. Tentzeris (S'94–M'98–SM'03–F'10) received the Diploma degree *(magna cum laude)* in electrical and computer engineering from the National Technical University of Athens, Athens, Greece, and the M.S. and Ph.D. degrees in electrical engineering and computer science from the University of Michigan, Ann Arbor, MI, USA.

He was a Visiting Professor with the Technical University of Munich, Munich, Germany, in 2002, a Visiting Professor with GTRI-Ireland, Athlone, Ireland, in 2009, and a Visiting Professor with LAAS-CNRS, Toulouse, France, in 2010. He heads the Agile Technologies for High-Performance Electromagnetic Novel Applications Research Group (20 researchers), Georgia Institute of Technology, Atlanta, GA, USA. He has served as the Head of the GT-ECE Electromagnetics Technical Interest Group, the Georgia Electronic Design Center Associate Director of the RFID/Sensors Research, the Georgia Tech NSF-Packaging Research Center Associate Director of the RF Research, and the RF Alliance Leader. He is currently a Ken Byers Professor of flexible electronics with the School of Electrical and Computer Engineering, Georgia Institute of Technology. He has authored over 650 papers in refereed journals and conference proceedings, five books, and 25 book chapters. He holds 14 patents. He has given over 100 invited talks to various universities and companies all over the world. He has helped develop academic programs in 3-D/inkjet-printed RF electronics and modules, flexible electronics, origami and morphing electromagnetics, highly integrated/multilayer packaging for RF and wireless applications using ceramic and organic flexible materials, paper-based RFIDs and sensors, wireless sensors and biosensors, wearable electronics, green electronics, energy harvesting and wireless power transfer, nanotechnology applications in RF, microwave MEMS, and SOP-integrated (ultrawideband, multiband, mmW, and conformal) antennas.

Dr. Tentzeris is a member of the URSI-Commission D, the MTT-15 Committee, and the Technical Chamber of Greece, an Associate Member of EuMA, and a Fellow of the Electromagnetic Academy. He was a recipient/co-recipient of the 1997 Best Paper Award from the International Hybrid Microelectronics and Packaging Society, the 2000 NSF CAREER Award, the 2001 ACES Conference Best Paper Award, the 2002 International Conference on Microwave and Millimeter-Wave Technology Best Paper Award (Beijing, China), the 2002 Georgia Tech-ECE Outstanding Junior Faculty Award, the 2003 NASA Godfrey Art Anzic Collaborative Distinguished

Publication Award, the 2003 IBC International Educator of the Year Award, the 2003 IEEE CPMT Outstanding Young Engineer Award, the 2004 IEEE TRANSACTIONS ON ADVANCED PACKAGING Commendable Paper Award, the 2006 IEEE MTT Outstanding Young Engineer Award, the 2006 Asia–Pacific Microwave Conference Award, the 2007 IEEE APS Symposium Best Student Paper Award, the 2007 IEEE IMS Third Best Student Paper Award, the 2007 ISAP 2007 Poster Presentation Award, the 2009 IEEE TRANSACTIONS ON COMPONENTS AND PACKAGING TECHNOLOGIES Best Paper Award, the 2009 E. T. S. Walton Award from the Irish Science Foundation, the 2010 IEEE Antennas and Propagation Society Piergiorgio L. E. Uslenghi Letters Prize Paper Award, the 2010 Georgia Tech Senior Faculty Outstanding Undergraduate Research Mentor Award, the 2011 International Workshop on Structural Health Monitoring Best Student Paper Award, the 2012 FiDiPro Award in Finland, the iCMG Architecture Award of Excellence, the 2013 IET Microwaves, Antennas and Propagation Premium Award, the 2014 Georgia Tech ECE Distinguished Faculty Achievement Award, the 2014 IEEE RFID-TA Best Student Paper Award, the 2015 IET Microwaves, Antennas and Propagation Premium Award, the 2016 Bell Labs Award Competition 3rd Prize, the 2017 Georgia Tech Outstanding Achievement in Research Program Development Award, and the 2017 Archimedes IP Salon Gold Medal. He was the TPC Chair of the IEEE MTT-S IMS 2008 Symposium and the Chair of the 2005 IEEE CEM-TD Workshop. He is also the Vice Chair of the RF Technical Committee (TC16) of the IEEE CPMT Society. He is also the Founder and the Chair of the RFID Technical Committee (TC24) of the IEEE MTT-S and the Secretary/Treasurer of the IEEE C-RFID. He served as the IEEE MTT-S Distinguished Microwave Lecturer from 2010 to 2012 and the IEEE CRFID Distinguished Lecturer. He is also an Associate Editor of the IEEE TRANSACTIONS ON MICROWAVE THEORY AND TECHNIQUES, IEEE TRANSACTIONS ON ADVANCED PACKAGING, and *International Journal of Antennas and Propagation*.

Luca Roselli (M'92–SM'01–F'18) joined the University of Perugia, Perugia, Italy, in 1991. In 2000, he founded the spin-off WiS Srl, Foligno, Italy. He was involved in electronic technologies for the Internet of Things for six years. He is currently a Qualified Full Professor with the University of Perugia, where he teaches applied electronics and coordinates the High Frequency Electronics Laboratory. He has authored over 280 papers (H-i 28, i10 82, and over 3000 citations in Scholar) and *Green RFID Systems* (Cambridge Univ. Press, 2014). His current research interests include HF electronic systems with special attention to RFID, new materials, and wireless power transfer.

Dr. Roselli was a member of the Board of Directors of ART Srl, Urbino, Italy, from 2008 to 2012. He is also a member of the list of experts of the Italian Ministry of Research, the past Chair of the IEEE Technical Committees MTT-24-RFID, the Vice Chair of 25-RF Nanotechnologies, 26-Wireless Power Transfer, the ERC Panel PE7, and the Advisory Committee of the IEEE-WPTC, and the Chairman of the SC-32 of IMS. He is also the Co-Chair of the IEEE Wireless Sensor Network Conference. He organized the VII Computational Electromagnetic Time Domain in 2007 and the first IEEE Wireless Power Transfer Conference in 2013. He is also an Associate Editor of the *IEEE Microwave Magazine*. He is involved on the boards of several international conferences. He is also a reviewer for many international journals, including the PROCEEDINGS OF THE IEEE, IEEE TRANSACTIONS ON MICROWAVE THEORY AND TECHNIQUES, and IEEE MICROWAVE AND WIRELESS COMPONENTS LETTERS.